

The Extended *Chandra* Deep Field South Survey: X-ray Point-Source Catalog

Shanil N. Virani, Ezequiel Treister^{1,2}, and C. Megan Urry¹

Department of Astronomy, Yale University, P.O. Box 208101, New Haven, CT 06520

svirani@astro.yale.edu

ABSTRACT

The Extended *Chandra* Deep Field South (E-CDF-S) survey consists of 4 *Chandra* ACIS-I pointings and covers ≈ 1100 square arcminutes (≈ 0.3 deg²) surrounding the original CDF-S field to a depth of approximately 228 ks. This is the largest *Chandra* survey ever conducted at such depth and only one XMM-Newton survey reaches a lower flux limit in the hard 2.0–8.0 keV band. We detect 642 unique sources, of which 532 are detected in the full 0.5–8.0 keV band, 480 in the soft 0.5–2.0 keV band, and 334 in the hard 2.0–8.0 keV band. For point sources near the aim point, the limiting fluxes are approximately 1.8×10^{-16} erg cm⁻² s⁻¹ and 7.8×10^{-16} erg cm⁻² s⁻¹ in the 0.5–2.0 keV and 2.0–8.0 keV bands, respectively. We present the differential and cumulative flux distributions, which are in good agreement with the number counts from previous deep X-ray surveys and with the predictions from an AGN population synthesis model that can explain the X-ray background. In general, fainter sources have harder X-ray spectra, consistent with the hypothesis that these sources are mainly obscured AGN.

Subject headings: diffuse radiation — surveys — cosmology: observations — galaxies: active — X-rays: galaxies — X-rays: general.

¹Yale Center for Astronomy and Astrophysics, Yale University, P.O. Box 208121, New Haven, CT 06520

²Departamento de Astronomía, Universidad de Chile, Casilla 36-D, Santiago, Chile.

1. Introduction

Wide-area X-ray surveys have played a fundamental role in understanding the nature of the sources that populate the X-ray universe. Early surveys like the *Einstein* Medium Sensitivity Survey (Gioia et al. 1990), the ROSAT International X-ray/Optical Survey (Ciliegi et al. 1997), and the ASCA Large Sky Survey (Akiyama et al. 2000) showed that the vast majority of the X-ray sources are active galactic nuclei (AGNs). More specifically, shallow wide-area surveys in the soft (0.5–2.0 keV) X-ray band yield mostly unobscured, broad-line AGNs, which are characterized by a soft X-ray spectrum with a photon index of $\Gamma \simeq 1.9$ (Nandra & Pounds 1994). In contrast, deep X-ray surveys — particularly surveys that make use of the unprecedented, sub-arcsecond spatial resolution of the *Chandra* X-ray Observatory — find AGN with harder X-ray spectra ($\Gamma \sim 1.4$) at fainter fluxes, more like the hard spectrum of the X-ray background.

Deep *Chandra* surveys have thus opened a new vista on resolving the X-ray background and identifying the role and evolution of accretion power in all galaxies. The cosmic X-ray background is now almost completely resolved (~ 70 – 90%) into discrete sources in the deep, pencil beam surveys like the *Chandra* Deep Fields (CDF-N, Brandt et al. 2001; CDF-S, Giacconi et al. 2002). To understand the composition of the sources that make up the X-ray background, population synthesis models have been constructed (Madau et al. 1994; Comastri et al. 1995; Gilli et al. 1999; Gilli et al. 2001; Treister & Urry 2005) which typically require approximately 3 times as many obscured AGN as traditional Type 1 AGN.

While the deep fields provide the deepest view of the X-ray universe and have generated plentiful AGN samples at lower luminosities, the small area covered by pencil-beam surveys means luminous sources are poorly sampled. In an attempt to determine the luminosity function of X-ray emitting AGN up to $z \sim 5$, as well as to leverage existing deep multiwavelength data in the extended $30' \times 30'$ field centered on the CDF-S, the region surrounding the CDF-S was recently observed by *Chandra*. Covering ≈ 1100 square arcminutes (≈ 0.3 deg²), the E-CDF-S is the largest *Chandra* survey field at this depth (≈ 230 ks), and is the second deepest and widest survey ever conducted in the X-rays (the XMM-Newton survey of the Lockman Hole (Hasinger 2004) is deeper in the hard band and has $\sim 30\%$ more area).

In this paper, we present the X-ray catalog for the E-CDF-S and the number counts in two energy bands. In subsequent papers, we will present the optical and near-IR properties of these X-ray sources, including first results from our deep optical spectroscopy campaign obtained as part of the one-square-degree MUltiwavelength Survey by Yale/Chile (MUSYC) (Gawiser et al. 2005).

In Section 2, we describe our data reduction procedure. In Section 3, we describe the

point source detection and astrometry. The X-ray source catalog and basic survey results are presented in Section 4 and the conclusions are given in Section 5. The average Galactic column density along this line of sight for the four pointings is $9.0 \times 10^{20} \text{ cm}^{-2}$ (Stark et al. 1992). $H_0 = 70 \text{ km s}^{-1} \text{ Mpc}^{-1}$, $\Omega_M = 0.3$, and $\Omega_\Lambda = 0.7$ are adopted throughout this paper which is consistent with the cosmological parameters reported by Spergel et al. (2003). All coordinates throughout this paper are J2000.

2. Observations and Data Reduction

2.1. Instrumentation and Diary of Observations

All nine observations of the E-CDF-S survey field were conducted with the Advanced CCD Imaging Spectrometer (ACIS) on-board the *Chandra* X-ray Observatory³ as part of the approved program (proposal number 05900218) of PI Niel Brandt. ACIS consists of 10 CCDs, distributed in a 2×2 array (ACIS-I) and a 1×6 array (ACIS-S). All 4 of the ACIS-I CCDs are front-illuminated (FI) CCDs; 2 of the 6 ACIS-S CCDs are back-illuminated CCDs (S1 and S3). Of these 10 CCDs, at most 6 can be operated at any one time. Table 1 presents a journal of the *Chandra* observations of the E-CDF-S. All nine observations were conducted in VERY FAINT mode (See the *Chandra* Proposers’ Guide, pg. 102) so that the pixel values of the 5×5 event island are telemetered rather than just the 3×3 event island as in FAINT mode. This telemetry format offers the advantage of further reducing the instrument background after ground processing (see Section 2.2). Observation ids (ObsIds) 5019–5022 and 6164 also had the ACIS-S2 CCD powered on (see Table 1). However, due to the large off-axis angle of the S2 CCD during these observations, it has a much broader point spread function (PSF) and hence lower sensitivity so we exclude data from this CCD and focus only on data collected from the ACIS-I CCDs. The on-axis CCD for each ACIS-I observation is I3 and the ACIS-I field of view is $16'9 \times 16'9$.

2.2. Data Reduction

All data were re-processed using the latest version of the *Chandra* Interactive Analysis of Observations⁴ (CIAO; Version 3.2.1; released 10 February 2005) software as well as version

³For additional information on the ACIS and *Chandra* see the *Chandra* Proposers’ Guide at <http://cxc.harvard.edu/udocs/docs/>.

⁴see <http://cxc.harvard.edu/ciao/>.

3.0.0 of the calibration database (CALDB; released 12 December 2004). We chose to re-reduce all nine datasets rather than simply use the standard data processing (SDP) level 2 event files because we wanted the datasets to be reduced in a consistent manner, and more importantly, we wanted to take advantage of better *Chandra* X-ray Center (CXC) algorithms to reduce the ACIS particle background by using the information located in the outer 16 pixels of the 5×5 event island⁵, as well as executing a new script that is much more efficient at identifying ACIS “hot pixels” and cosmic ray afterglow events⁶. This new hot pixel and cosmic ray afterglow tool is now implemented in the standard data processing pipeline at the CXC but was not applied in the SDP pipeline of the present observations.

The following procedure was used to arrive at a new “level 2” event file. Before applying the new CIAO tool to identify ACIS “hot pixels and cosmic ray afterglow events,” the pixels identified in the CXC-provided level 1 event file as being due to a cosmic ray afterglow event were reset. An “afterglow” is the residual charge from the interaction of a cosmic ray in a front-side illuminated CCD frame. Some of the excess charge is captured by charge traps created by the radiation damage suffered early in the mission (see Townsley et al. 2000 and references therein) and released over the next few to a few dozen frames. If these afterglow events are not removed from the data, they can result in the spurious “detection” of faint sources. To better account for such events, a new, more precise method for identifying afterglow events was developed by the CXC and has now been introduced into the standard data processing pipeline. This CIAO tool, “`acis_run_hotpix`,” was then run on the reset level 1 event file to identify and flag hot pixels and afterglow events in all 9 ACIS observations of the E-CDF-S. The last step in producing the new level 2 event file was to run the CIAO tool “`acis_process_events`.” In addition to applying the newest gain map supplied in the latest release of the CALDB, this tool also applies the pixel randomization and the ACIS charge transfer inefficiency (CTI) correction. The latter corrects the data for radiation damage sustained by the CCDs early in the mission. All of these corrections are part of the standard data processing and are “on” by default in `acis_process_events`. The time-dependent gain correction is also applied to the event list to correct the pulse-invariant (PI) energy channel for the secular drift in the average pulse-height amplitude (PHA) values. This drift is caused primarily by gradual degradation of the CTI of the ACIS CCDs (e.g., Schwartz & Virani 2004). Finally, the observation-specific bad pixel map created by “`acis_run_hotpix`” was supplied, and the option to clean the ACIS particle background by making use of the additional pixels telemetered in VERY FAINT mode was turned on.

⁵See “Reducing ACIS Quiescent Background Using Very Faint Mode”, <http://cxc.harvard.edu/cal/Acis/Calprods/vfbgrnd/index.html>.

⁶See <http://cxc.harvard.edu/ciao/threads/acishotpixels/>.

Once a new level 2 event file was produced, we applied the standard grade filtering to each observation, choosing only event grades 0, 2, 3, 4, and 6 (the standard *ASCA* grade set), and the standard Good Time Intervals supplied by the SDP pipeline. We also restrict the energy range to 0.5–8.0 keV, as the background rises steeply below and above those limits⁷. Lastly, we examined the background light curves for all 9 observations as the ACIS background is known to vary significantly. For example, Plucinsky & Virani (2000) found that the front-illuminated CCDs can show typical increases of 1 - 5 cts s⁻¹ above the quiescent level, while the back-illuminated CCDs can show large excursions — as high as 100 cts s⁻¹ above the quiescent level — during these “background flares”. The durations of these intervals of enhanced background are also highly variable, ranging from 500 s to 10⁴ s. The cause of these background flares is currently not known (see Grant, Bautz, & Virani 2002); however, they may be caused by low-energy protons (<100 keV; e.g., Plucinsky & Virani 2000; Struder et al. 2001). The time periods corresponding to these background flares are generally excised from the data before proceeding with further analysis although not always (see Brandt et al. 2001; Nandra et al. 2005). In fact, Kim et al. (2004) find that the source detection probability depends strongly on the background rate. To examine our observations for such periods, we used the CIAO script `ANALYSE_LTCRV.SL` which identifies periods where the background is $\pm 3\sigma$ above the mean. All of the 9 observations were filtered according to this prescription (see Table 1 for a comparison of raw exposure time vs. filtered exposure time); this procedure resulted in only ≈ 40.6 ks ($\approx 4\%$) being lost due to background flares (954.2 ks vs. 913.6 ks). Of this, 20.3 ks were excluded from the end ObsID 5017 due to a flare in which the count rate increased by a factor of ≈ 2 . Table 2 lists the net exposure time for each of the 4 pointings used to image the E-CDF-S region. The net exposure time for each of the 4 pointings varies from a low of 205 ks to a high of 239 ks, with the mean net exposure time for the entire survey field of 228 ks.

3. Data Analysis

In this paper, we report on the sources detected in three standard X-ray bands (see Table 3): 0.5–8.0 keV (full band), 0.5–2.0 keV (soft band), and 2.0–8.0 keV (hard band). The raw ACIS resolution is 0.492 arcsec pixel⁻¹, however, source detection and flux determinations were performed on the block 4 images, *i.e.*, 1.964 arcsec pixel⁻¹, as the source detect tool and exposure map generation require significant computer resources for full size images.

⁷See <http://cxc.harvard.edu/contrib/maxim/stowed/>.

3.1. Image and Exposure Map Creation

Observations at each of the four pointings were combined via the CIAO script “merge_all.” This script was executed using CIAO version 2.3 because of a known bug in the “asphist” tool under CIAO version 3.2.1; this bug results in incorrect exposure maps for the merged image⁸. At each pointing, the observation with the longest integration time was used for co-ordinate registration. For example, when merging ObsIds 5015 and 5016, the merged event list was registered to ObsId 5015 as it has approximately twice the integration time as 5016. Table 2 lists the ObsIds used for each pointing and the net integration time. For each pointing, we constructed images in the three standard bands: 0.5–8.0 keV (full band), 0.5–2.0 keV (soft band), and 2.0–8.0 keV (hard band); see Table 3. The soft and full band raw images for the entire survey field are presented in Figures 1 and 2, respectively⁹.

We constructed exposure maps in these three energy bands for each pointing and for the entire survey field. In Figure 2, we show the full band exposure map for the entire survey field¹⁰. These exposure maps were created in the standard way and are normalized to the effective exposure of a source location at the aim point. The procedure used to create these exposure maps accounts for the effects of vignetting, gaps between the CCDs, bad column filtering, and bad pixel filtering. However, it should be noted that “charge blooms” caused by cosmic rays can reduce the detector efficiency by as much as few percent¹¹. There is currently no way to account for such charge cascades; however, when a tool becomes available, we will correct for this effect if necessary and make the new exposure maps publicly available at the World Wide site listed in Footnote 8. The exposure maps were binned by 4 so that they were congruent to the final reduced images. Lastly, a photon index of $\Gamma = 1.4$, the slope of the X-ray background in the 0.5–8.0 keV band (e.g. Marshall et al. 1980; Gendreau et al. 1995; Kushino et al. 2002) was used in creating these exposure maps. In Figure 4, we show the cumulative plot of the survey solid angle versus flux for the soft and hard bands. The total survey area is found to be ≈ 1100 arcmin² (≈ 0.3 deg²).

⁸See the usage warning at http://cxc.harvard.edu/ciao/threads/merge_all/.

⁹Raw and adaptively smoothed *ASCA* -grade images for all three standard bands (See Table 3) are available from <http://www.astro.yale.edu/svirani/ecdfs/>.

¹⁰Exposure maps for all three standard bands (see Table 3) are available from <http://www.astro.yale.edu/svirani/ecdfs/>.

¹¹See <http://cxc.harvard.edu/ciao/caveats>.

3.2. Point Source Detection

To perform X-ray source detection, we applied the CIAO wavelet detection algorithm *wavdetect* (Freeman et al. 2002). Although several other methods have been used in other survey fields to find sources in *Chandra* observations (e.g., Giacconi et al. 2002; Nandra et al. 2005), we chose *wavdetect* to allow a straightforward comparison between sources found in our catalog with those found in the CDF-S (Giacconi et al. 2002; Alexander et al. 2003). Moreover, *wavdetect* is more robust in detecting individual sources in crowded fields and in identifying extended sources than the other CIAO detection algorithm, *celldetect*. Point-source detection was performed in each standard band (see Table 3) using a “ $\sqrt{2}$ sequence” of wavelet scales; scales of 1, $\sqrt{2}$, 2, $2\sqrt{2}$, 4, $4\sqrt{2}$, and 8 pixels were used. Brandt et al. (2001), for example, showed that using larger scales can detect a few additional sources at large off-axis angles but found that this “ $\sqrt{2}$ sequence” gave the best overall performance across the CDF-N field. Moreover, as Alexander et al. (2003) point out, sources found with larger scales tend to have source properties and positions too poorly defined to give useful results.

Our criterion for source detection is that a source must be found with a false-positive probability threshold (p_{thresh}) of 1×10^{-7} in at least one of the three standard bands. This false-positive probability threshold is typical for point-source catalogs (e.g., Alexander et al. 2003; Wang et al. 2004), although Kim et al. (2004) found that a significance threshold parameter of 1×10^{-6} gave the most efficient results in the *Chandra* Multiwavelength Project (ChaMP) survey. Running *wavdetect* with the lower ChaMP significance threshold parameter for the E-CDF-S dataset yielded many spurious sources in visual tests. Executing *wavdetect* with a low false-positive probability threshold and then performing *post facto* processing of the detected sources to attempt to separate true sources from spurious sources would be subjective and counter to the philosophy of *wavdetect*, as Freeman et al. (2002) and Brandt et al. (2001) point out. Clearly, our detection criterion is conservative in that fainter but real sources may be present in our field but not tabulated in our catalog. For the remaining source detection parameters, we used the default values specified in CIAO which included requiring that a minimum of 10% of the on-axis exposure was needed in a pixel before proceeding to analyze it. We also applied the exposure maps generated for each pointing at an energy of 1.4 keV (see Section 3.1) to mitigate finding spurious sources which are most often located at the edge of the field of view.

The number of spurious sources per pointing is approximately $p_{thresh} \times N_{pix}$, where N_{pix} is the total number of pixels in the image, according to the *wavdetect* documentation. Since there are approximately 2×10^6 pixels in each image for each pointing, we expect ~ 0.2 spurious sources per pointing per band. Therefore, treating the 12 images searched as

independent, we expect ~ 2 -3 false sources in our catalog (Table 4) for the case of a uniform background. Of course the background is neither perfectly uniform nor static as the level decreases in the gaps between the CCDs and increases slightly near bright point sources. As mentioned by Brandt et al. (2001) and Alexander et al. (2003), one might expect the number of false sources to be increased by a factor of ≈ 2 -3 due to the large variation in effective exposure time across the field and the increase in background near bright sources due to the PSF “wings”. But our false-source estimate is likely to be conservative by a similar factor since *wavdetect* suppresses fluctuations on scales smaller than the PSF. That is, a single pixel is unlikely to be considered a source detection cell — particularly at large off-axis angles (Alexander et al. 2003).

The source lists generated by the procedure above for each of the standard bands in each of the pointings of the E-CDF-S were merged to create the point-source catalog presented in Table 4. The source positions listed in the catalog are the full band *wavdetect*-determined positions except when the source was detected only in the soft or hard bands. To identify the same source in the different energy bands, a matching radius of $2\times$ the PSF size of each detect cell was used. With this method, 9 and 3 soft- and hard-band sources, respectively, have more than 1 counterpart. We therefore take the closest one. Note that Table 4 excludes sources found by *wavdetect* in which one or both of the axes of the “source ellipse” collapsed to zero. Hornschemeier et al. (2001) find that using the *wavdetect*-determined counts for such objects results in a gross underestimate of the number of counts even though the source was detected with a probability threshold of 1×10^{-7} .

Below we define the columns in Table 4, our catalog of sources found in the E-CDF-S survey.

- Column 1 gives the ID number of the source in our catalog. Sources are listed in order of right ascension.
- Column 2 indicates the International Astronomical Union approved names for the sources in this catalog. All sources begin with the acronym “CXO ECDFS”¹².
- Columns 3 and 4 give the right ascension and declination, respectively. These are *wavdetect*-determined positions. If a source is detected in multiple bands, then we quote the position determined in the full band; when a source is not detected in the full band we use, in order of priority, the soft-band position then the hard-band position.

¹²Name registration submitted to <http://cdsweb.u-strasbg.fr/viz-bin/DicForm>.

- Column 5 gives the PSF cell size, in units of arcseconds, as determined by *wavdetect*. The larger the PSF size, the farther off-axis the source lies.
- Columns 6, 7, and 8 give the count rates (in units of cts s^{-1}) in the full band as well as the corresponding upper and lower errors estimated according to the prescription of Gehrels (1986). If a source is undetected in this band, no count rate is tabulated.
- Columns 9, 10, and 11 give the count rates (in units of cts s^{-1}) in the soft band as well as the corresponding upper and lower errors estimated according to the prescription of Gehrels (1986). If a source is undetected in this band, no count rate is tabulated.
- Columns 12, 13, and 14 give the count rates (in units of cts s^{-1}) in the hard band as well as the corresponding upper and lower errors estimated according to the prescription of Gehrels (1986). If a source is undetected in this band, no count rate is tabulated.
- Column 15 lists the full band flux (in units of $\text{erg cm}^{-2} \text{s}^{-1}$) calculated using a photon slope of $\Gamma = 1.4$ and corrected for Galactic absorption. If a source was undetected in the full band but was detected in the hard or soft band, the hard- or soft- band flux (in that order of priority) was used to extrapolate to the full band assuming a photon slope of 1.4.
- Column 16 lists the soft band flux (in units of $\text{erg cm}^{-2} \text{s}^{-1}$) calculated using a photon slope of $\Gamma = 1.4$ and corrected for Galactic absorption. If a source was undetected in the soft band but was detected in the full or hard band, the full- or hard- band flux (in that order of priority) was used to extrapolate to the soft band assuming a photon slope of 1.4.
- Column 17 lists the hard band flux (in units of $\text{erg cm}^{-2} \text{s}^{-1}$) calculated using a photon slope of $\Gamma = 1.4$ and corrected for Galactic absorption. If a source was undetected in the hard band but was detected in the full or soft band, the full- or soft- band flux (in that order of priority) was used to extrapolate to the hard band assuming a photon slope of 1.4.
- Column 18 provides individual notes for each source. Examples include the catalog ID (c#) if detected in the CDF-S by Alexander et al. (2003), or if the source was selected from a band other the full band ('h' or 's') or only detected in the full band ('f').

To determine source counts for each of our sources, we extracted counts in the standard bands from each of the images using the geometry of the *wavdetect* source cell and the *wavdetect*-determined source position. For example, to determine the counts in the soft

band, we used the position and geometry determined by *wavdetect* in the soft band image to extract soft band counts. Net count rates were then calculated using the effective exposure (which includes vignetting) for each pointing (exposure maps generated as described in Section 3.1). Errors were derived following Gehrels (1986), assuming a 84% confidence level. Note that the exposure maps do account for the degradation of the soft X-ray response of ACIS due to the build-up of a contamination layer on the ACIS optical blocking filter (e.g. Marshall et al. 2004; see Section 3.4). Therefore, the count rates reported in Table 4 are exposure- and contamination-corrected.

In Table 5 we summarize the source detections in the three standard bands, and in Table 6 we summarize the number of sources detected in one band but not in another. To convert the count rates to flux, we determined the conversion factor for each band assuming a photon slope of $\Gamma = 1.4$ and the mean Galactic N_H absorption along the line-of-sight for each of the 4 pointings ($N_H = 9 \times 10^{20} \text{ cm}^{-2}$; Stark et al. 1992).

Our faintest soft-band sources have ≈ 4 counts (about one every 1.5 days), and our faintest hard-band sources have ≈ 6 counts; these sources are detected near the aim point. The corresponding 0.5–2.0 keV and 2–8 keV flux limits, corrected for the Galactic column density, are $\approx 1.8 \times 10^{-16} \text{ erg cm}^{-2} \text{ s}^{-1}$ and $\approx 7.8 \times 10^{-16} \text{ erg cm}^{-2} \text{ s}^{-1}$, respectively. Of course, these flux limits vary and generally increase across the field of view.

Undoubtedly, there are some sources in Table 4 that are extended sources (*i.e.*, resolved by *Chandra*). Giacconi et al. (2002) find 18 extended sources in their 1 Ms catalog of the CDF-S out of 346 unique sources. The E-CDF-S survey has approximately 25% the integration time of the CDF-S but is approximately 3 times larger in area. Therefore, we expect roughly the same fraction of our sources reported in Table 4 are likely to be extended. The identification, X-ray, and optical properties of these sources will be presented in a later paper.

3.3. Astrometry

Given the superb *Chandra* spatial resolution, the on-axis positional accuracy is often quoted as being accurate to within $1''$ (e.g., Kim et al. 2004); in fact, the overall 90% uncertainty circle of a *Chandra* X-ray absolute position has a radius of 0.6 arcsec, and the 99% limit on positional accuracy is 0.8 arcsec¹³. Nevertheless, as the off-axis angle increases, the PSF broadens and becomes circularly asymmetric (see *Chandra* Proposer’s Guide; URL

¹³<http://cxc.harvard.edu/cal/ASPECT/celmon/>.

listed in Footnote 1). Therefore, source positions for faint sources at large off-axis angles may not be accurate. In order to test the astrometry of the *wavdetect*-determined positions, we have matched our full band X-ray positions provided in Table 4 against deep *BVR*-band imaging produced by the Multiwavelength Survey by Yale/Chile (MUSYC¹⁴; Gawiser et al. 2005). The 5σ depth of the MUSYC optical imaging of this field is 27.1 mag with approximately $0.''85$ seeing. Briefly, by correlating the X-ray positions reported in Table 4 with the optical positions found for sources in the E-CDF-S field, we find that approximately 66% of the full band sources reported here have an optical counterpart within $1.''5$ of the X-ray position. Furthermore, in comparing the X-ray positions with the optical positions for these matched sources, we find a mean offset of $-0.''08$ in RA and $+0.''28$ in Dec. (We do not correct the X-ray positions for these offsets.) The optical properties of these X-ray sources will be presented in a forthcoming paper (Virani et al. 2005b, in prep.).

3.4. Accuracy of Source Detections and Fluxes

Approximately one third of the E-CDFS field overlaps with the 1 Ms *Chandra* Deep Field South (see Figure 2 for the field layout). This is very useful as it allows us to compare our results with the properties of the overlapping sources already published. In particular, we used the catalog of Alexander et al. (2003), obtained by re-analyzing the original CDF-S data. In Figure 5 we show the ratio of our fluxes to those reported by Alexander et al. (2003) for the overlapping sources. For this comparison, neither the CDF-S nor the E-CDFS sources were corrected for intrinsic Galactic absorption. (This correction is $\simeq 4\%$ in the soft band and is negligible in the hard band.)

Sources were matched using the closest CDF-S counterpart to each E-CDFS source, using a maximum search radius of $\sim 2''$. Excluding the most discrepant top and bottom 15% of the sources, our fluxes are $\sim 4\%$ higher in the soft band and $\sim 7.8\%$ lower in the hard band. In the first case, the difference can be explained by the different treatment of the contamination layer, which is particularly important in the soft band. The Alexander et al. (2003) catalog used ACISABS¹⁵ to correct their fluxes for the presence of a contamination layer in the ACIS instrument. This tool assumes a spatially-uniform contamination layer composed of hydrogen, carbon, nitrogen, and oxygen. However, recent analysis of grating data (Marshall et al. 2004) shows that the amount of contamination correction depends on the spatial position on the instrument, and that the actual composition of the contamination

¹⁴For more information: <http://www.astro.yale.edu/musyc/>.

¹⁵Available at <http://www.astro.psu.edu/users/chartas/xcontdir/xcont.html>

is hydrogen, carbon, oxygen, and fluorine (P. Plucinsky, priv. comm.). These two new discoveries may have caused Alexander et al. (2003) to underestimate the contamination correction, thus making their fluxes lower in the soft band. In the hard band, the discrepancy can be explained by our assumed value of $\Gamma = 1.4$ for the spectral slope to calculate fluxes, while Alexander et al. (2003) used individual spectral fits for most of these overlapping sources. We conclude that the fluxes are broadly consistent and that systematic uncertainties in their average values are $\leq 10\%$, although individual fluxes have larger uncertainties (and some AGN may actually have varied).

4. Results and Discussion

We found 642 unique sources in the Extended *Chandra* Deep Field-South survey field which spans $\approx 0.3 \text{ deg}^2$ on the sky. Of these, 532 were detected in the 0.5–8.0 keV full band, 480 in the 0.5–2.0 keV soft band, and 334 in the 2.0–8.0 keV hard band. There are 37 hard band sources that are not detected in either the soft or full bands, 72 soft band sources are not detected in either the hard or full bands, and 78 full band sources are not detected in either the soft or hard bands. Of the 334 hard-band sources, 84 were not detected in the soft band ($\sim 25\%$). These are candidates for highly absorbed sources. Of the 480 and 334 sources detected in the soft and hard bands, respectively, 118 and 73 are detected in the CDF-S itself. Over this 0.11 deg^2 area, with an exposure time of $\sim 1 \text{ Ms}$, Giacconi et al. (2002) found 346 unique sources, of which 307 were detected in the 0.5–2.0 keV band and 251 in the 2–10 keV band. In the CDF-N, with an area similar to the CDF-S but with twice the exposure, Alexander et al. (2003) found 503 X-ray sources in the 2 Ms exposure. The number of sources found in the E-CDF-S is consistent with these two pencil beam surveys after accounting for differences in exposure time and area.

The cumulative distribution of sources for the soft and the hard bands is shown in Figure 6. Error bars in the cumulative log N–log S relation are correlated. Error bars for a given bin were calculated by adding in quadrature the error bars from the previous bin to the 84% confidence error bars appropriate to the additional number of sources in the present bin, following the procedure described in Gehrels (1986). The observed distribution is compared to the compilation of Moretti et al. (2003) and to the log N–log S for the *Chandra* deep fields reported by Bauer et al. (2004). In the soft band there is very good agreement with the comparison sample in the flux range from $\sim 4 \times 10^{-14}$ to $2 \times 10^{-16} \text{ erg cm}^{-2}\text{s}^{-1}$. At the bright end, the discrepancy is not statistically significant, $\sim 1\sigma$, because there are few bright X-ray sources in our field. At fluxes below $\sim 2 \times 10^{-16} \text{ erg cm}^{-2}\text{s}^{-1}$, the observed log N–log S relation flattens relative to the comparison sample because of the incompleteness of

our dataset near the flux limit. Sources with soft fluxes of $\sim 2 \times 10^{-16}$ erg cm $^{-2}$ s $^{-1}$ are only detected at the $\sim 2\sigma$ level, and thus not all sources will be recovered. The log N–log S relation for the hard band is shown in the right panel of Figure 6 and is compared again with the distributions of Moretti et al. (2003) and Bauer et al. (2004). Moretti et al. (2003) used 2–10 keV instead of 2–8 keV for the hard band. To convert 2–10 keV fluxes to the 2–8 keV band, we used a factor of 0.8, corresponding to the flux conversion assuming a $\Gamma=1.4$ spectral slope. Bauer et al. (2004) quote 2–8 keV but appear to have used 2–10 keV, so we also converted their fluxes by the same factor (which reproduces their curve in Figure 4). As in the soft band, very good agreement with previously reported log N–log S relations is seen for the 8×10^{-14} – 2×10^{-15} erg cm $^{-2}$ s $^{-1}$ range, and again the low number of sources at the bright end and incompleteness at the faint end explain the observed discrepancies.

The differential log N–log S for both the soft and hard bands is shown in Figure 7. These observed distributions are compared to the predictions of the AGN population synthesis model of Treister & Urry (2005) which explains the X-ray background as a superposition of mostly obscured AGN. This model also explains the multiwavelength number counts of AGN in the *Chandra* Deep Fields (Treister et al. 2004). Given that these models match very well the observed cumulative flux distributions from existing surveys, it is not surprising that this model also successfully explains the log N–log S distributions in the E-CDFS field. The only discrepancies can be found at the fainter end, where as in the cumulative flux distribution case, incompleteness in the observed sample causes the number of observed sources to fall below the model prediction.

One of the early *Chandra* results was the finding that fainter X-ray sources have in general harder spectra (Giacconi et al. 2001), represented by a higher values of the hardness ratio. Figure 8 shows that this effect is also observed in the E-CDF-S field, for a much larger number of sources. This trend is explained by obscuration since the soft band count rate is relatively more affected than the hard band, creating a harder observed X-ray spectrum while at the same time reducing the observed soft flux. This is in accordance with the general picture of AGN unification, although the precise geometry is not constrained, and it is as expected from population synthesis models (e.g., Treister & Urry 2005 and references therein) which require a large number of obscured AGN at moderate redshift to explain the spectral shape of the X-ray background.

5. Conclusions

We present here the catalog of X-ray properties for the sources detected in deep *Chandra* observations of the E-CDFS field, the largest *Chandra* survey ever performed in terms of

both area and depth. This survey covers a total of 0.3 square degrees, roughly 3 times the area of each very deep *Chandra* Deep Field. A total of 642 unique sources were detected in the four ACIS-I pointings in this field; 73 sources were detected in the soft but not in the full band, while 37 were detected only in the hard band. Roughly 20% of these 642 unique sources — 118 sources in the soft band and 73 in the hard band — were previously detected in the CDF-S. The fluxes derived for these sources agree well with the fluxes obtained from the CDF-S observations.

The X-ray log N–log S in the soft and hard bands agree well with those derived from other X-ray surveys and with predictions of the most recent AGN population synthesis models for the X-ray background.

As first discovered in early deep *Chandra* observations, we find in this sample that faint X-ray sources have in general harder spectra, indicating that these sources are likely obscured AGN at moderate redshifts. This is predicted by AGN unification models that explain the properties of the X-ray background. A future paper will discuss the optical and near-IR properties of these objects. This field was observed with the *Spitzer* Space Telescope by the MIPS GTO team and will also be observed by *Spitzer* as part of an approved program related to the MUSYC survey (PI: P. van Dokkum).

The source catalog and images presented in this paper are available in electronic format on the World Wide Web (<http://www.astro.yale.edu/svirani/ecdfs>). We will continue to improve the source catalog as better calibration information, analysis methods, and software become available. For example, we plan to optimize the searching for variable sources and study the multiwavelength properties of these X-ray sources. Improved searching for diffuse sources will be performed as the *Chandra* background becomes better understood.

We are extremely grateful to Samantha Stevenson of the CXC Help Desk for her help and patience in answering our many questions regarding CIAO-related tools. We also acknowledge the help of Eric Gawiser and Jeffrey Van Duyne in cross-correlating the X-ray and optical positions. ET would like to thank the support of Fundación Andes, Centro de Astrofísica FONDAF and the Sigma-Xi foundation through a Grant in-aid of Research. This work was supported in part by NASA grant HST-GO-09425.13-A.

REFERENCES

- Akiyama, M., et al. 2000, ApJ, 532, 700
Alexander, D. M., et al. 2003, AJ, 126, 539

- Barger, A. J., et al. 2003, AJ, 126, 632
- Bauer, F. E., Alexander, D. M., Brandt, W. N., Schneider, D. P., Treister, E., Hornschemeier, A. E., & Garmire, G. P. 2004, AJ, 128, 2048
- Brandt, W. N., et al. 2001, AJ, 122, 2810
- Ciliegi, P., Elvis, M., Wilkes, B. J., Boyle, B. J., & McMahon, R. G. 1997, MNRAS, 284, 401
- Comastri, A., Setti, G., Zamorani, G., & Hasinger, G. 1995, A&A, 296,1
- Freeman, P. E., Kashyap, V., Rosner, R., & Lamb, D. Q. 2002, ApJS, 138 185
- Gawiser, E., et al. 2005, submitted to ApJS.
- Gendreau, K. C., et al. 1995, PASJ, 47, L5
- Gehrels, N., 1986, ApJ, 303, 336
- Giacconi, R., et al. 2001, ApJ, 551, 624
- Giacconi, R., et al. 2002, ApJS, 139, 369
- Gilli, R., Risaliti, G., & Salvati, M. 1999, A&A, 347, 424
- Gilli, R., Salvati, M., & Hasinger, G. 2001, A&A, 366, 407
- Gioia, I. M., Maccacaro, T., Schild, R. E., Wolter, A., Stocke, J. T., Morris, S. L., & Henry, J. P. 1990, ApJS, 72, 567
- Grant, C. E., Bautz, M. W., & Virani, S. N. 2002, ASP Conf. Ser. 262, The High Energy Universe at Sharp Focus: *Chandra* Science, ed. E. M. Schlegel & S. D. Vrtilik (San Francisco: ASP), 401.
- Hasinger, G. 2004, Nuc. Phys. B (Proc. Supp.), 132, 86
- Hornschemeier, A. E., et al. 2001, ApJ, 554, 742
- Kim, D.-W., et al. 2004, ApJS, 150, 19
- Kushino, A., et al. 2002, PASJ, 54, 237
- Madau, P., Ghisellini, G., & Fabian, A. C. 1994, MNRAS, 270, L17+
- Marshall, F. E., et al. 1980, ApJ, 235 4

- Marshall, H. E., et al. 2004, SPIE, 5165, 497
- Moretti, A., Campana, S., Lazzati, D., & Tagliaferri, G. 2003, ApJ, 588, 696
- Nandra, K., & Pounds, K. A. 1994, MNRAS, 268, 405
- Nandra, K., et al. 2005, MNRAS, 356, 568
- Plucinsky, P. P. & Virani, S. N. 2000, SPIE, 4012, 681
- Schwartz, D. A., & Virani, S. N. 2004, ApJ, 615, L21
- Spergel, D. N., et al. 2003, ApJS, 148, 175
- Stark, A. A., Gammie, C. F., Wilson, R. W., Bally, J., Linke, R. A., Heiles, C., & Hurwitz, M. 1992, ApJS, 79, 77
- Struder, L., et al. 2001, A&A, 365, 18
- Szokoly, G. P., et al. 2004, ApJS, 155, 271
- Townsley, L. K., Broos, P. S., Garmire, G. P., & Nousek, J. A. 2000, ApJ, 534, L139
- Treister, E., et al. 2004, ApJ, 616, 123
- Treister, E., & Urry, C.M. 2005, ApJ, in press, astro-ph/0505300
- Wang, J. X., et al. 2004, ApJ, 608, 21

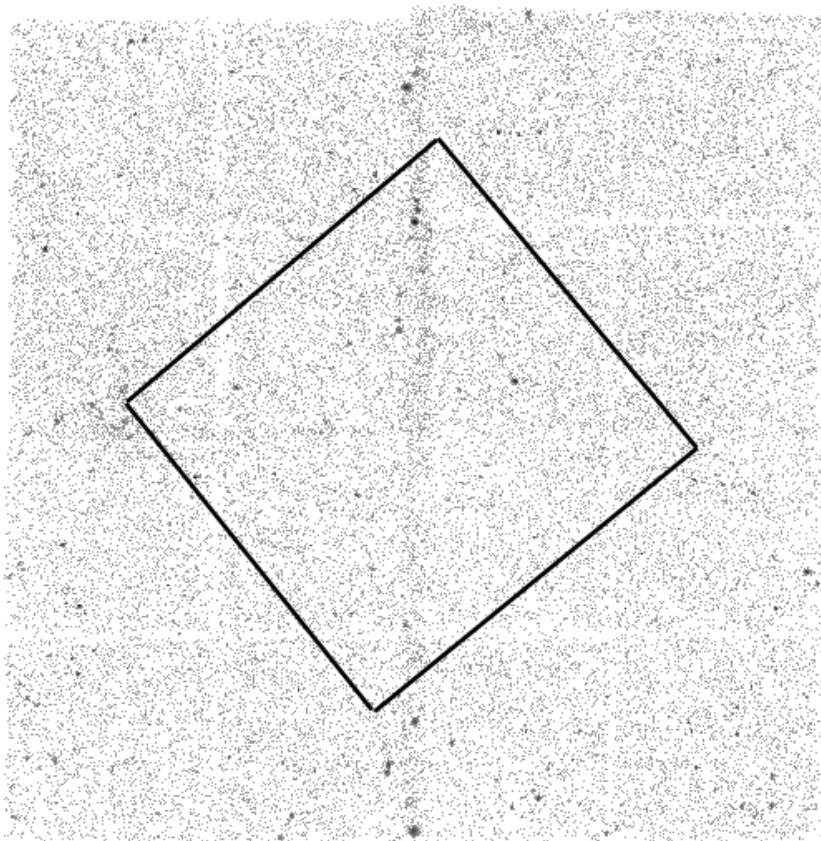


Fig. 1.— Raw soft band image of the E-CDF-S. This image has been binned by a factor of four in both RA and Dec, and has been made using the standard *ASCA* grade set. The light grooves running through the image correspond to the gaps between the ACIS-I CCDs. The black square superimposed on the raw image is the approximate footprint of the CDF-S proper (Giacconi et al. 2002).

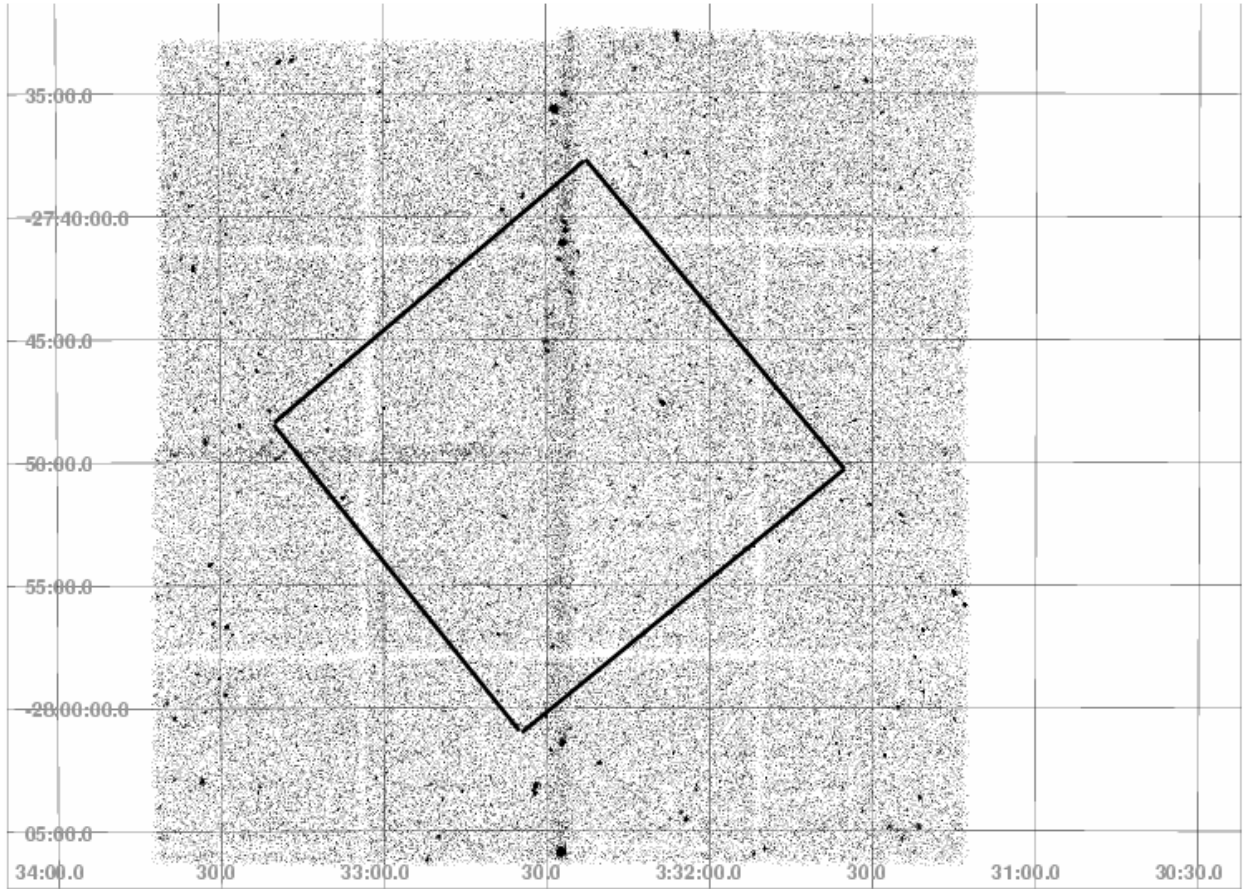


Fig. 2.— Raw full band (0.5–8.0 keV) image of the E-CDF-S. This image has been binned by a factor of four in both RA and Dec, and has been made using the standard *ASCA* grade set. The light grooves running through the image correspond to the gaps between the ACIS-I CCDs. The black square superimposed on the raw image is the approximate footprint of the CDF-S proper (Giacconi et al. 2002).

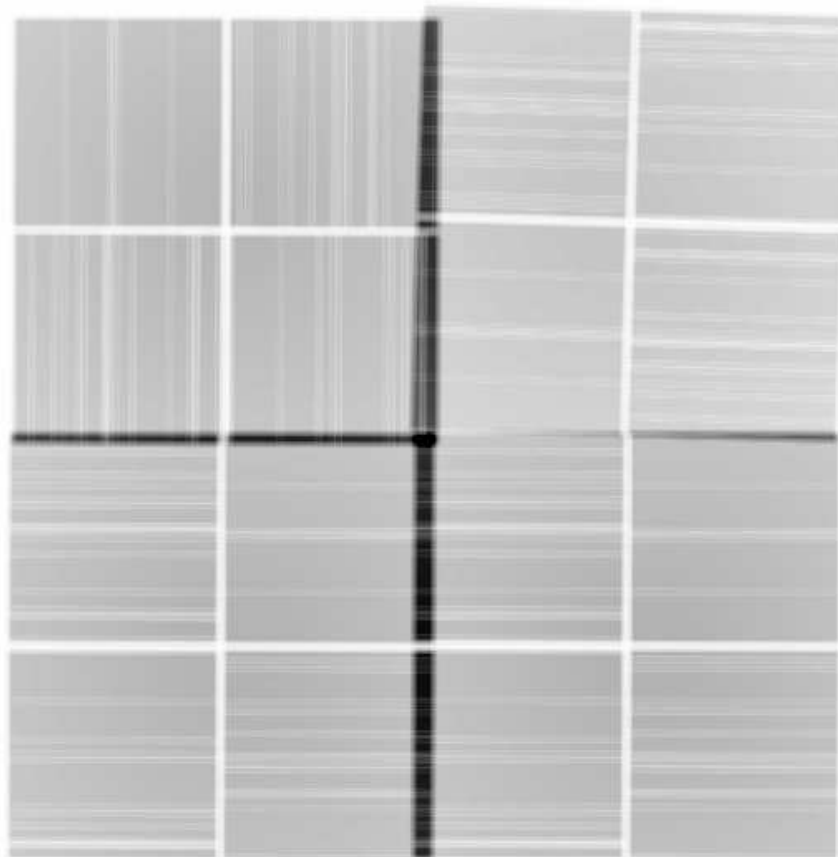


Fig. 3.— Full-band exposure map for the combined 9 exposures of the E-CDF-S, computed for monochromatic incident X-rays with energy of 1.4 keV. This image has been binned by a factor of four in both RA and Dec. Exposure maps for the other energy bands are available from the World Wide Web site listed in Footnote 8.

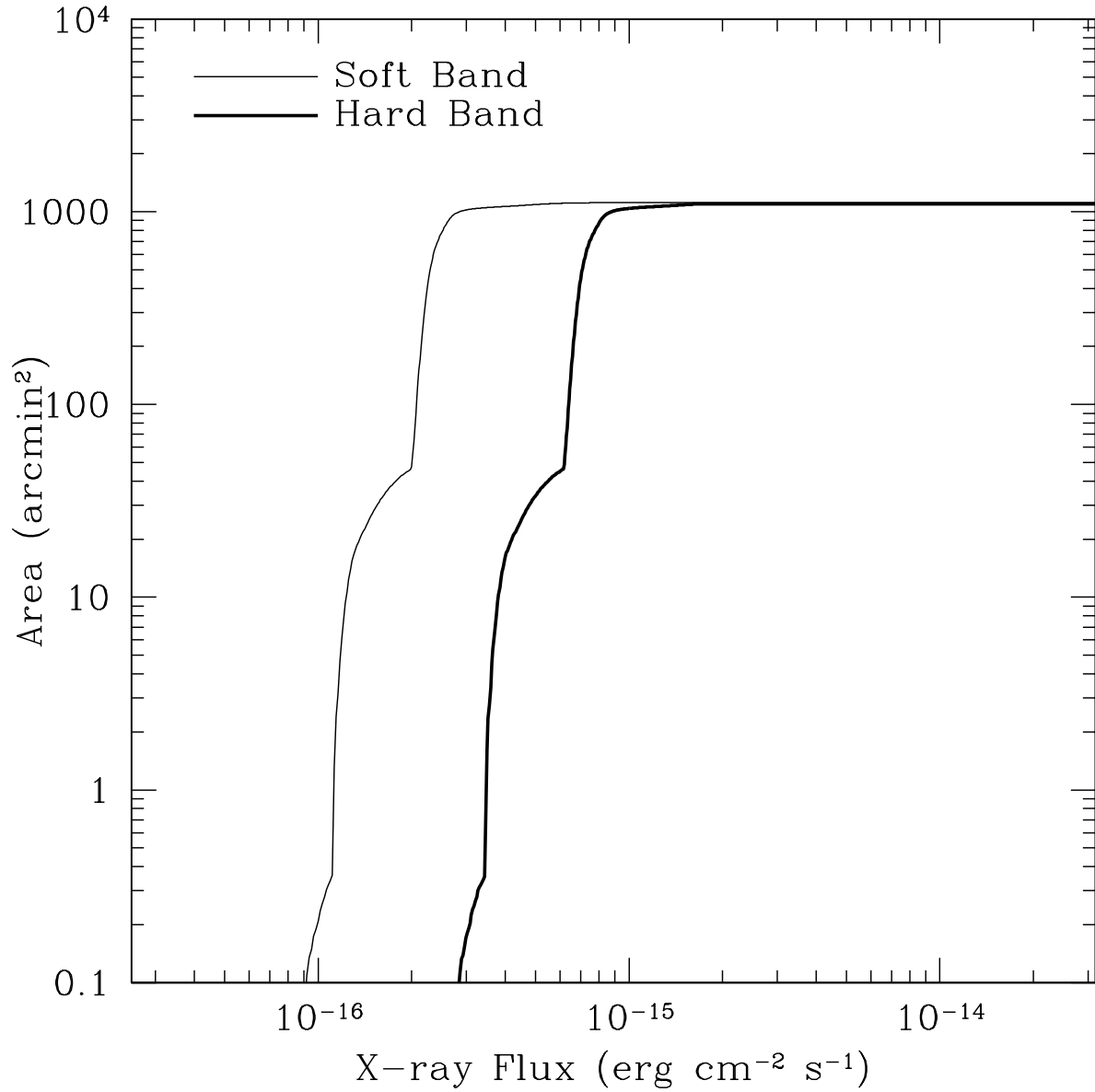


Fig. 4.— The survey area vs. limiting flux for the two bands for which we have calculated the log N -log S function: soft band (*thin line*) and the hard band (*thick line*). The total area of the survey is ≈ 1100 arcmin² (~ 0.3 deg²).

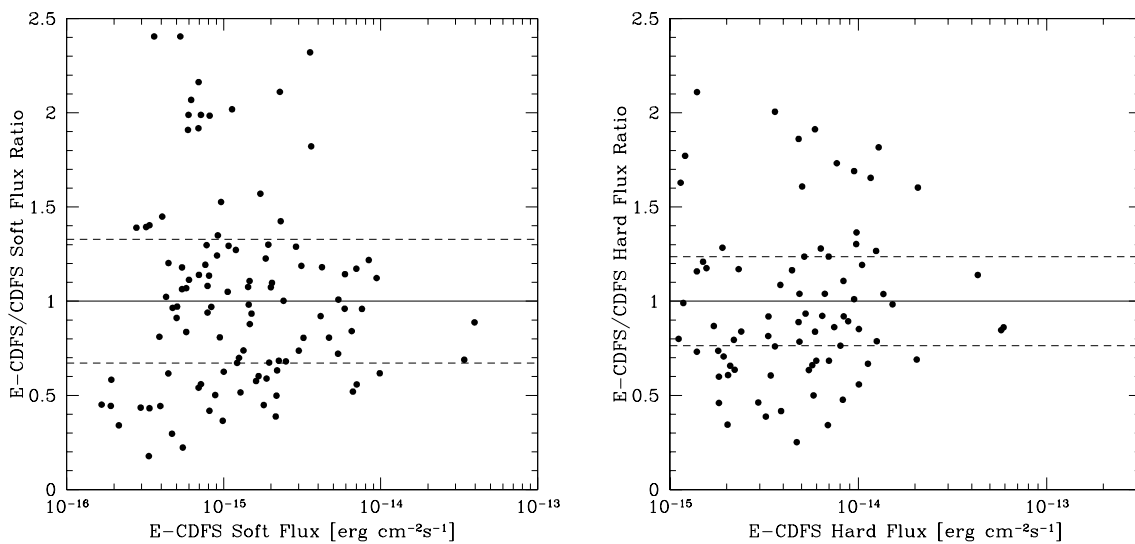


Fig. 5.— Comparison of X-ray fluxes for the 115 sources (*left panel*) and the 89 hard sources (*right panel*) detected in the CDF-S catalog of Alexander et al. (2003). For this comparison, X-ray fluxes are not corrected for intrinsic Galactic absorption. In general, there is very good agreement between the two independent data sets, with an average flux ratio in the soft band of 1.04, with an RMS of 33%, shown by the dashed horizontal lines. In the hard band the average flux ratio is 0.922 with an RMS of 23%. This indicates that systematic uncertainties in the flux are $< 10\%$.

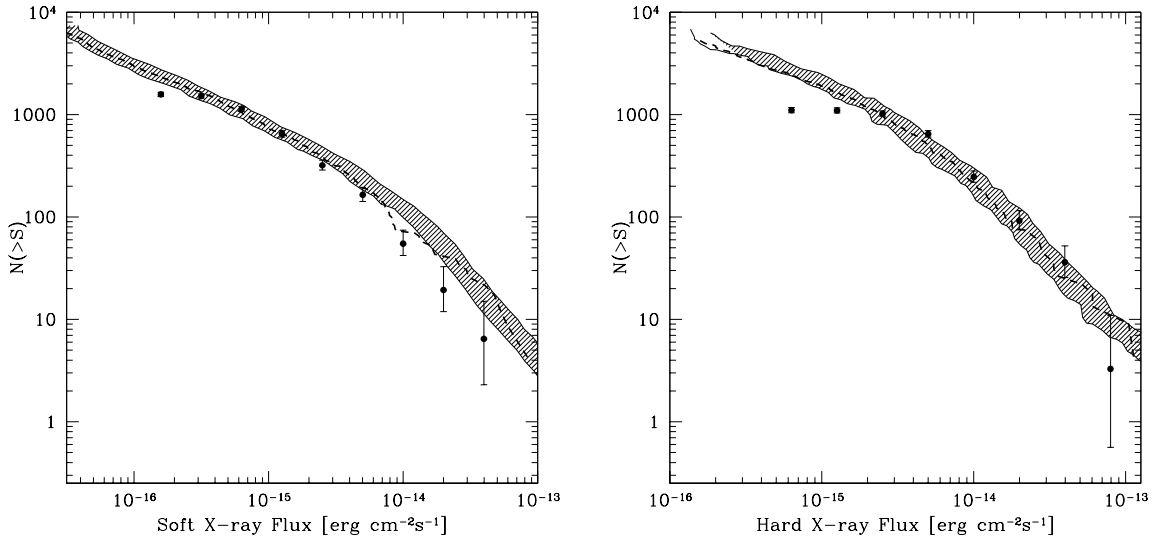


Fig. 6.— Cumulative flux distributions for the soft (*left panel*) and hard (*right panel*) bands. (*filled circles:*) present data for the E-CDF-S catalog, with error bars corresponding to the 84% confidence level (Gehrels 1986). Note that the error bars are not independent. For comparison, we show the log N–log S compiled by Moretti et al. (2003) (from ROSAT, ASCA, XMM, and *Chandra* observations) with $\pm 1\sigma$ errors (*hashed region*), and the distribution for sources in the *Chandra* Deep Fields North and South (Bauer et al. 2004; *dashed line*). The 2–10 keV fluxes of Moretti et al. (2003) and Bauer et al. (2004) were converted to 2–8 keV fluxes using a factor of 0.8, corresponding to a spectral slope of 1.4.

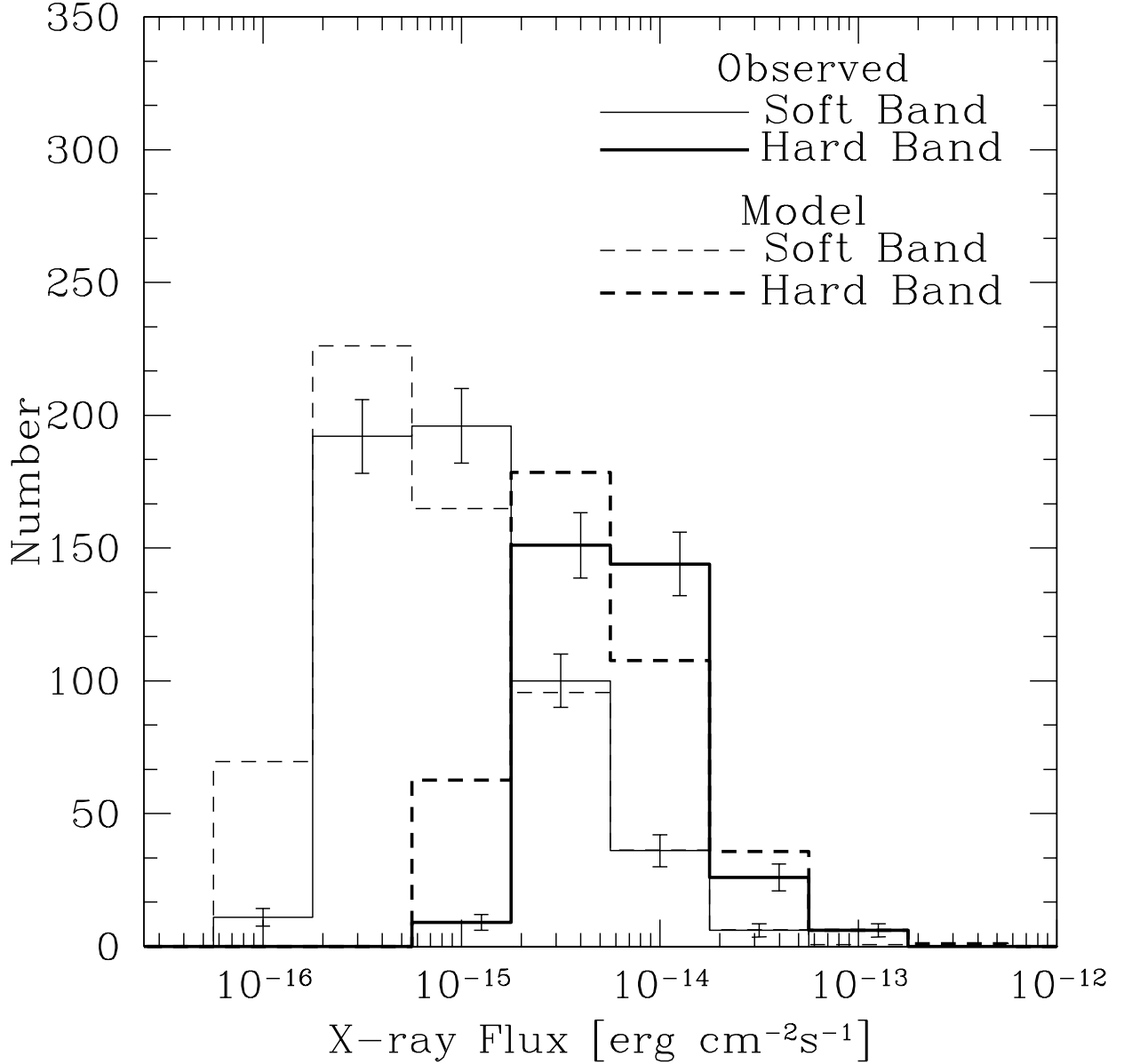


Fig. 7.— *Solid lines*: Differential flux distribution for sources in the E-CDFS in the soft (*thin line*) and hard (*thick line*) bands, in $\Delta \log S=0.5$ bins. *Dashed lines*: The distribution predicted by an AGN unification model that also explains the X-ray background (Treister et al. 2004, Treister & Urry 2005) agrees well in the bright to intermediate flux range for both bands. Below $F_X \sim 3 \times 10^{-16}$ erg cm⁻² s⁻¹ in the soft band, and $F_X \sim 2 \times 10^{-15}$ erg cm⁻² s⁻¹ in the hard band, incompleteness in our catalog becomes important.

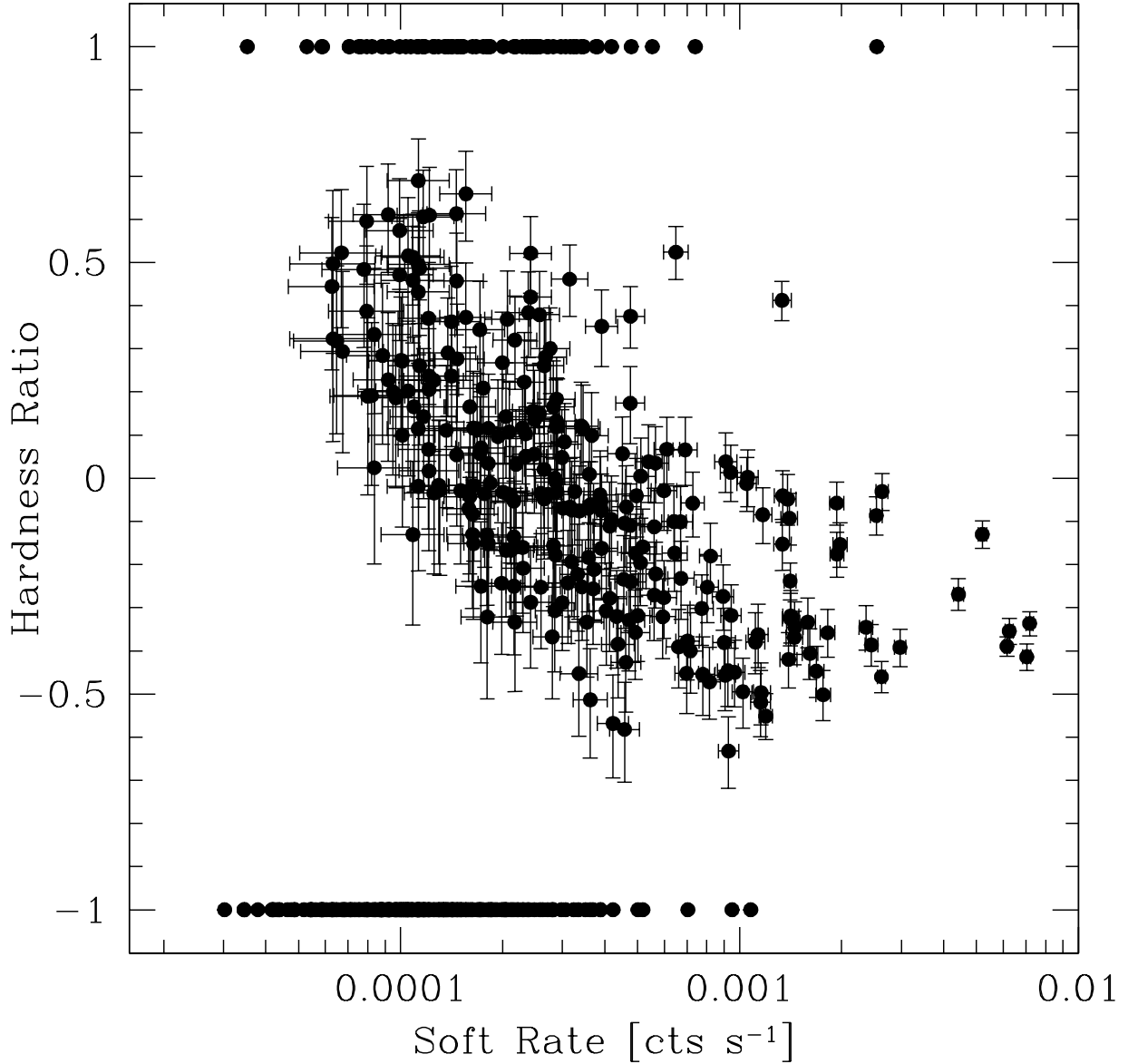


Fig. 8.— Hardness ratio (defined as the ratio of hard minus soft counts to the summed counts) versus soft X-ray count rate for sources in the E-CDFS. Error bars correspond to 84% confidence level on the count rates (Gehrels 1986). For sources not detected in the soft band (i.e., HR=+1), the hard count rate was used instead. Fainter sources in the soft band have harder X-ray spectra, supporting the hypothesis that these sources are mainly obscured AGN, as required by population synthesis models for the X-ray background.

Table 1. Journal of *Chandra* Observations of the E-CDF-S

Obs. ID	Obs. Start	Exposure Time (ks)		Aim Point			Roll Angle (degrees)	CCDs Clocked
		Raw	Filtered	α_{2000}	δ_{2000}			
5015	29 Feb 2004	162.9	154.8	03 33 05.61	-27 41 08.84		270.2	I0–I3
5016	03 Mar 2004	77.2	76.8	03 33 05.61	-27 41 08.88		270.2	I0–I3
5017	14 May 2004	155.4	135.2	03 31 51.43	-27 41 38.80		181.5	I0–I3
5018	16 May 2004	72.0	70.2	03 31 51.43	-27 41 38.79		181.5	I0–I3
5019	17 Nov 2004	163.1	162.3	03 31 49.94	-27 57 14.56		0.2	I0–I3,S2
5020	15 Nov 2004	77.6	76.9	03 31 49.94	-27 57 14.56		0.2	I0–I3,S2
5021	13 Nov 2004	97.8	94.2	03 33 02.93	-27 57 16.08		0.2	I0–I3,S2
5022	15 Nov 2004	79.1	75.8	03 33 02.94	-27 57 16.07		0.2	I0–I3,S2
6164	20 Nov 2004	69.1	67.8	03 33 02.93	-27 57 16.04		0.2	I0–I3,S2

Table 2. Net Exposure Time Per Pointing

Pointing	Obsids	Net Exposure (ks)
Northeast	5015, 5016	231.6
Northwest	5017, 5018	205.4
Southeast	5021, 5022, 6164	237.4
Southwest	5019, 5020	239.2
Mean		228.4

Table 3. Definition of Energy Bands and Hardness Ratio

Name	Definition
Full Band (F)	0.5–8.0 keV
Soft Band (S)	0.5–2.0 keV
Hard Band (H)	2.0–8.0 keV
Hardness Ratio (HR)	$(H - S)/(H + S)$

Table 4. Catalog of X-ray sources in the E-CDFS field.

ID	Name CXO-E-CDFS-	RA	Dec	PSF "	Count Rate: Full Band			Count Rate: Soft Band			Count Rate: Hard Band			FB Flux ^a	SB Flux ^a erg cm ⁻² s ⁻¹
		J2000				value	upper	lower	value	upper	lower	value	upper		
1	J033335.6-273935	03 33 35.56	-27 39 35.3	1.75	7.64e-04	8.26e-04	7.07e-04	5.05e-04	5.56e-04	4.59e-04	—	—	—	9.16e-15	2.95e-15
2	J033334.9-274209	03 33 34.93	-27 42 08.5	1.64	9.00e-03	9.20e-03	8.80e-03	—	—	—	2.88e-03	3.00e-03	2.77e-03	1.08e-13	3.30e-14
3	J033332.9-274011	03 33 32.92	-27 40 11.2	1.45	2.16e-04	2.51e-04	1.85e-04	1.94e-04	2.28e-04	1.65e-04	—	—	—	2.59e-15	1.14e-15
4	J033332.8-274908	03 33 32.79	-27 49 08.0	4.05	1.81e-03	1.91e-03	1.73e-03	1.06e-03	1.13e-03	9.95e-04	4.45e-04	4.93e-04	4.01e-04	2.17e-14	6.21e-15
5	J033329.8-274009	03 33 29.84	-27 40 09.1	1.17	3.45e-04	3.89e-04	3.07e-04	1.81e-04	2.14e-04	1.54e-04	—	—	—	4.14e-15	1.06e-15

Note. — This table is published in its entirety in the electronic edition of the Journal. A portion is shown here for guidance regarding its form and content.

^aFlux: Corrected for Galactic absorption with $N_H = 9 \times 10^{19} \text{ cm}^{-2}$ assuming $\Gamma = 1.4$.

Table 5. Summary of *Chandra* Source Detections

Energy Band	Number of Sources ^a	Detected Counts Per Source			
		Maximum	Minimum	Median	Mean
Full Band	532	2401.6	4.6	53.0	124.8
Soft Band	488	1643.3	3.7	29.1	81.7
Hard Band	336	755.8	5.7	40.7	70.3

^aThere are 642 independent X-ray sources detected in total with a false-positive probability threshold of 1×10^{-7} , which means a 2–3 false sources may be expected in the catalog in Table 4.

Table 6. Sources Detected in One Band But Not Another

Detection Energy Band	Non-Detection Energy Band			
	Full	Soft	Hard	Neither
Full	0	125	236	78
Soft	73	0	230	72
Hard	38	84	0	37

Note. — For example, there were 125 sources detected in the full band but not in the soft band.